Geomechanics and Engineering, *Vol. 36, No. 5 (2024) 511-525*
https://doi.org/10.12989/gae.2024.36.5.511

Acoustic emission characteristics during damage-zone formation around a circular opening

Jong-Won Lee[1a], Eui-Seob Park[2b], Junhyung Choi[2c], Tae-Min Oh[**3] and Min-Jun Kim[*2]

[1]*Research Institute of Industrial Technology, Pusan National University, 2 Busandaehak-ro 63beon-gil, Geumjeong-gu, Busan 46241, Republic of Korea*
[2]*Deep Subsurface Storage & Disposal Research Center, Korea Institute of Geoscience and Mineral Resources (KIGAM), 124 Gwahak-ro, Yuseong-gu, Daejeon 34132, Republic of Korea*
[3]*Department of Civil and Environmental Engineering, Pusan National University, 2 Busandaehak-ro 63beon-gil, Geumjeong-gu, Busan 46241, Republic of Korea*

(*Received November 28, 2023, Revised February 23, 2024, Accepted February 24, 2024*)

Abstract. Underground openings significantly affect the mechanical stability of underground spaces and create damaged zones. This study investigated the acoustic emission (AE) characteristics associated with the formation of damaged zones around circular openings. Uniaxial compression experiments were conducted on three types of rock specimens, namely, granite (GN-1 and GN-2), gabbro (GB), and slate (SL), containing a circular opening. AE and digital image correlation (DIC) techniques were used to monitor and evaluate the damaged zones near the circular openings. The AE characteristics were evaluated using AE parameters, including count, energy, amplitude, average frequency, and RA value. The DIC results revealed that the estimated diameters of the damaged zones of GN-1, GN-2, GB, and SL were 1.66D, 1.53D, 1.49D, and 1.9D, respectively. The average displacements at the surface of the damaged zones for these specimens were 0.814, 0.786, 0.661, and 0.673 mm, respectively, thus demonstrating a strong correlation with Young's modulus. The AE analysis with DIC revealed that tensile failure occurred in the direction parallel to the maximum compression axis as the load increased. Thus, this study provides fundamental data for a comprehensive analysis of damaged zones in underground openings and will facilitate the optimization of rock engineering projects and safety assessments thereof.

Keywords: acoustic emission (AE); circular opening; damaged zone; digital image correlation (DIC)

1. Introduction

Underground openings are a critical factor in determining the mechanical stability of underground spaces. Owing to stress redistribution, a damaged zone can form near an underground openings and significantly degrade the stability of the underground space and performance of underground facilities. Consequently, evaluating the stability of underground openings containing damaged zones is crucial in rock mechanics research. To study the mechanical characteristics of underground openings, the basic configuration used is a circular opening, which is also the basic shape of a tunnel or mine cross-section. Extensive research has been conducted on theoretical models for rock mechanical behavior with corresponding numerical analysis studies (Fakhimi *et al*. 2002, Park *et al*. 2006, Wang *et al*. 2018, Hedayat and Weems 2019, Li *et al*. 2022a). These studies serve as a basis for further research and provide essential insights into the processes and factors that contribute to damaged zone formation. Although few experimental studies have been conducted on rock specimens containing circular openings to investigate fracture characteristics (Liu *et al*. 2015, Weng *et al*. 2018, Zhu *et al*. 2019), they are of considerable significance. The preliminary experimental studies revealed the most fundamental mechanisms related to the formation of a damaged zone around a circular opening and focused on the progressive fracturing processes of a circular opening. Nevertheless, there has been a paucity of studies that seek to quantitatively evaluate damaged zones using effective monitoring methods such as acoustic emission (AE) or digital image correlation (DIC) techniques.

AEs involve transient elastic waves that are generated when an external impact is applied, causing energy to be rapidly released and radiated from localized sources within a material (Oh *et al*. 2020). The AE technique has been extensively employed in rock mechanics research involving underground mining, tunnels, and underground space utilization, and serves as a monitoring system for detecting and locating rock damage (Kramadibrata *et al*. 2011, Hellier 2013, Ishida *et al*. 2017, Li *et al*. 2022b). Because the AE technique features passive characteristics that allow damage

∗Corresponding author, Senior Researcher
E-mail: kimmj@kigam.re.kr
**Corresponding author, Associate Professor
E-mail: geotaemin@pusan.ac.kr
[a]Ph.D., Post-Doctoral Researcher
E-mail: lee.j@pusan.ac.kr
[b]Ph.D., Head
E-mail: espark@kigam.re.kr
[c]Ph.D., Senior Engineer
E-mail: junhyung@kigam.re.kr

ISSN: 2005-307X (Print), 2092-6219 (Online)

to be detected prior to reaching critical failure (Grosse and Ohtsu 2008) and brittle failure mechanisms, such as microcracking, during rock fracturing experiments (Moradian *et al*. 2016, Hampton *et al*. 2018, Zhang *et al*. 2021, Du *et al*. 2022, Yoon *et al*. 2023), it plays an important role in monitoring and exploring rock mechanical behavior. Thus, the application of an AE monitoring system to evaluate a damaged zone is remarkably efficient, providing real-time monitoring data that can determine the stability of an underground opening.

Extensive studies have been conducted on the AE characteristics of rocks using conventional rock testing methods, such as uniaxial compression tests (Jin *et al*. 2017, Cao *et al*. 2019, Liu *et al*. 2021, Sun *et al*. 2023), tensile tests (Ma *et al*. 2020, Li *et al*. 2017, Guo *et al*. 2022a), and laboratory tests involving cores (Li *et al*. 2022c) or notched rock specimens (Gong *et al*. 2017, Guo *et al*. 2022b, Tang *et al*. 2020) under various failure modes. These studies have enhanced our understanding of the AE characteristics of rocks by analyzing AE parameters through the deformation and failure features of rock specimens. However, the corresponding AE characteristics exhibit patterns different from those of conventional rock specimens (Liu *et al*. 2021, Zha *et al*. 2021) because shear, tensile, and mixed-mode cracks all form in a complex pattern within the damaged zone around the circular opening (Liu *et al*. 2015). A good understanding of the AE characteristics of damaged zone formation could contribute positively to safety evaluations and the optimization of rock engineering project performances. However, there is a lack of experimental studies investigating AE characteristics during the formation of a damaged zone around a circular opening using AE parameter analyses. Therefore, in this study, uniaxial compression experiments were conducted on rock specimens with a circular opening to induce damaged zone formation using an AE monitoring system. The AE characteristics during the formation of the damaged zone were examined by analyzing the primary AE parameters and evaluating the crack mechanism near the circular opening. Furthermore, the DIC technique was used to evaluate the influential range of the damaged zone and verify the experimental results of the AE monitoring system. The findings of this study will provide fundamental data for enhancing the understanding of damaged zones in underground openings.

2. Materials and methods

2.1 Specimen preparation

Cubic blocks of rock with dimensions of 100 × 100 × 100 mm were used as specimens. These dimensions took into consideration the size of the load frame and installation positions of the AE sensors and cameras for the DIC technique. A cylindrical hole with a diameter of 20 mm was drilled into each block to create a circular opening in each specimen. Specimens from three types of rocks, namely, 2 Hwangdeung granite (GN-1 and GN-2), 1 Macheon gabbro (GB), and 1 Boryeong slate (SL), that are found in Korea were used in the experiments to investigate the influence of rock strength on damaged zone formation. To ensure the reliability of the experimental results for the granite specimen, which exhibits higher heterogeneity than the other specimens (Marshak 2019), the experiments were performed on two distinct granite samples. Basic property tests were conducted on the specimens to measure their P-wave velocity, Young's modulus, uniaxial compressive strength, and effective porosity, according to ASTM D2845-08, D7012-10, and D7063, respectively (ASTM 2008, ASTM 2010, ASTM 2011). The tests were performed for each rock type using five test specimens. Table 1 lists the mean values and standard deviations of the basic properties of the three rock types.

2.2 Test setup

A 160-ton material test system (MTS) with a 315-load frame, capable of servo-controlled loading and real-time displacement measurements, was used to apply the loading conditions to the specimens. To collect the AE data during the experiments, we installed and operated an AE monitoring system that included a controller, data acquisition device, AE sensors, and software package (AEwin for Express-8 E5.91 from MISTRAS). The AE sensor used in the experiment was a Nano 30, which exhibited a resonant response at 300 kHz and a favorable frequency response over the range of 125–750 kHz. The Nano 30 sensor was selected because AE signals are commonly observed within a frequency range of 100–2,000 kHz in laboratory experiments that examine rock fractures or deformations (Lockner 1993). Each sensor was equipped with a 2/4/6 preamplifier to obtain an amplification of 40 dB. The AE sensors were installed using high-vacuum grease to enhance the coupling performance at the interface between the rock and sensor. Four AE sensors were attached to the back surfaces of the specimens and positioned near the circular hole as the central reference point (Fig. 1(a)) to facilitate the DIC technique in the experiments. The sampling rate for AE signal acquisition was set to 1 MHz, and the acquisition threshold was established at an amplitude of 48 dB to minimize interference from mechanical and electromagnetic noise during the experiments. Based on the user manual (AEwin 2014), the AE time parameters were configured as follows: peak definition time = 200 μs, hit definition time = 800 μs, and hit lockout time = 1,000 μs. The connection statement of the AE sensors and performance of the source location were validated for each specimen before the experiments were conducted using the pencil lead-break test, which involved breaking a 0.5 mm pencil lead at predetermined locations.

After setting up the AE system, two Q-400 cameras equipped with Schneider Kreuznach lenses with a focal length of 12 mm were installed to capture images of the front surface of the specimens for DIC monitoring (Fig. 1(b)). Because the DIC technique is a measurement system for non-contact and full-field deformation analyses, the deformation and displacement of the surface of the specimen can be determined by analyzing the correlation

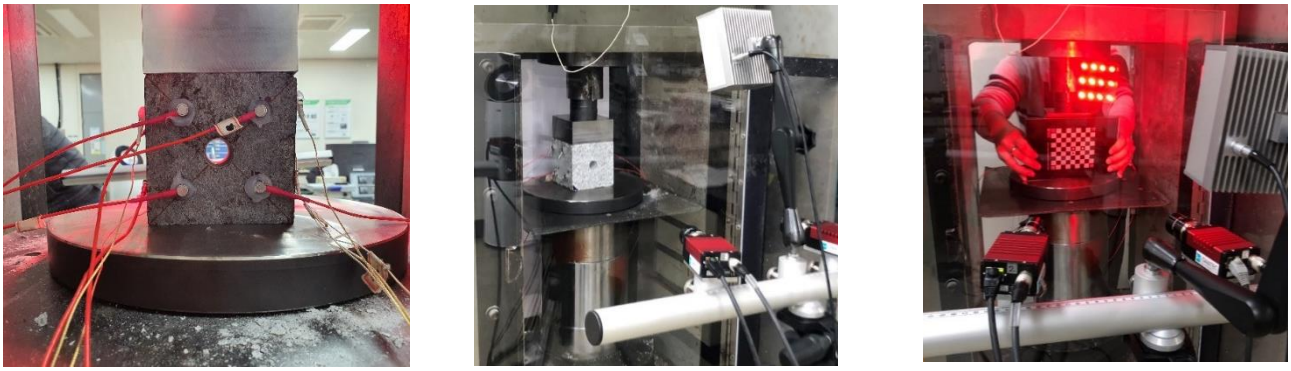

(a) Installation of AE sensors (b) Setting camera for DIC monitoring (c) Calibration for DIC monitoring

Fig. 1 Test setup for analyzing failure patterns using AE and DIC

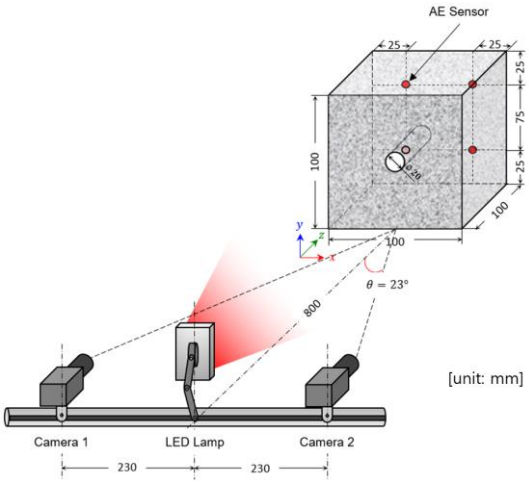

Fig. 2 Arrangement of the AE sensors and DIC camera for damage monitoring

Table 1 Basic properties of the test specimens

	Uniaxial compression strength (MPa)	Young's modulus (GPa)	Density (g/cm3)	P-wave velocity (m/s)
GB (Macheon Gabbro)	173.24 ± 19.26	57.32 ± 3.98	2.81 ± 0.01	5,200 ±351.64
GN (Hwang-deung Granite)	221.26 ± 18.84	45.32 ± 7.45	2.65 ± 0.01	3,192 ± 49.19
SL (Boryeong Slate)	314.52 ± 15.19	55.92 ± 5.25	2.70 ± 0.01	6,114 ± 35.78

between the speckle patterns within a region of interest in the captured images (Miao *et al*. 2021, Wu *et al*. 2021). The image data were acquired at a sampling rate of 2.5 Hz and processed using the ISTRA 4D software from Dantec Dynamics, in which a built-in algorithm tracked the movement of each speckle in the images to obtain the displacement measurements. Before starting the experiments, the entire system was calibrated using a special target matching the size of the specimens to determine the imaging parameters for software calculations, as shown in Fig. 1(c). The first captured image represented the initial state of the specimens, serving as a reference for the DIC analysis, and the images captured during the experiment were correlated with this reference image to obtain the strain and vector displacement measurements.

2.3 Test procedures

After successfully completing the setup process of the AE sensors and DIC cameras for the monitoring systems, the loading system was activated. An adapter pressure plate was placed between the spherical seat and specimen to ensure a uniform load was applied to the surface of the specimen. The AE, DIC, and loading systems were started simultaneously when the experiment commenced to synchronize the data processing. The loading rate was set to 0.005 mm/s, and the AE and DIC measurement data were monitored in real time (Fig. 2). The experiment was terminated once the pressure applied to the specimen reached 100 MPa. This limit was chosen because the primary objective of this experiment was to analyze the AE

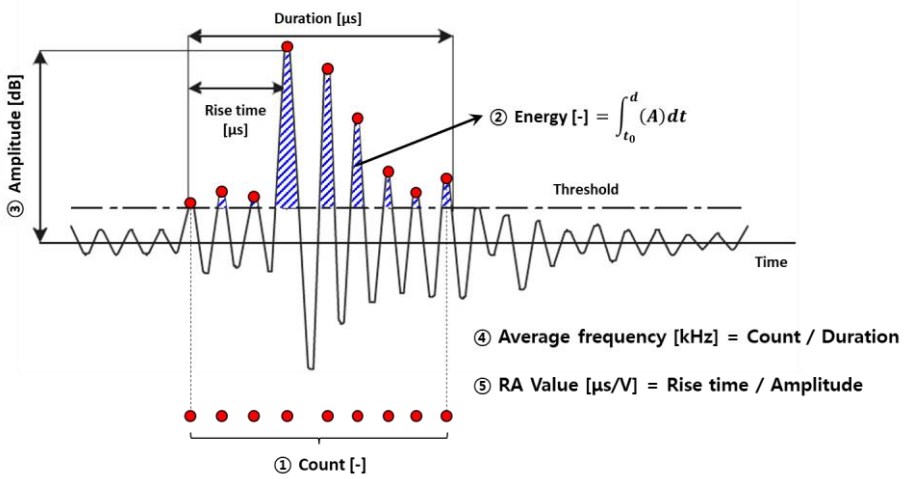

Fig. 3 Definition of AE parameters for analyzing the failure characteristics in a circular opening (Lee *et al*. 2020)

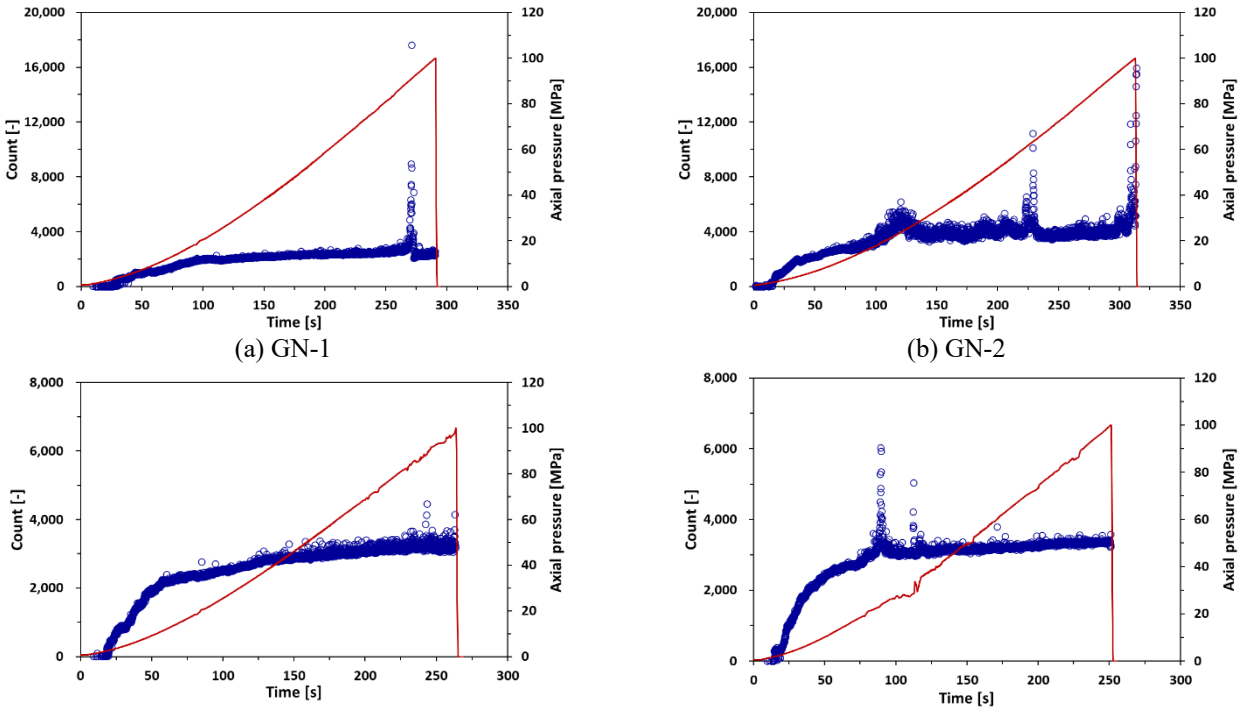

Fig. 4 Count results for all test specimens under axial pressure

and DIC data during the formation of the damaged zone, rather than assessing rock strength, failure criteria, or signals during the fracture process. The real-time monitoring of the image data collected from the DIC system during the experiment confirmed that an axial pressure of 100 MPa was sufficient to induce damaged zone formation around the circular opening.

3. AE parameter results and analysis

The analysis of the AE signals involved quantifying the measured signals based on their waveform and threshold relationships. Quantifying AE signals, also known as AE parameters, is a more useful approach for analyzing AE characteristics than directly analyzing complex AE waveforms. In this study, the failure characteristics of circular openings were explored by analyzing the AE parameters, including count, energy, amplitude, average frequency, and RA value (Fig. 3). Count, energy, and amplitude are commonly used to analyze the failure characteristics of rock media. The average frequency and RA values can also be used to identify failure modes, such as tensile or shear, in rock media. Therefore, as shown in Figs. 4-8, the parameters (marked by hollow circles) were plotted with the axial pressure (marked by a solid line) for all test specimens against the elapsed loading time.

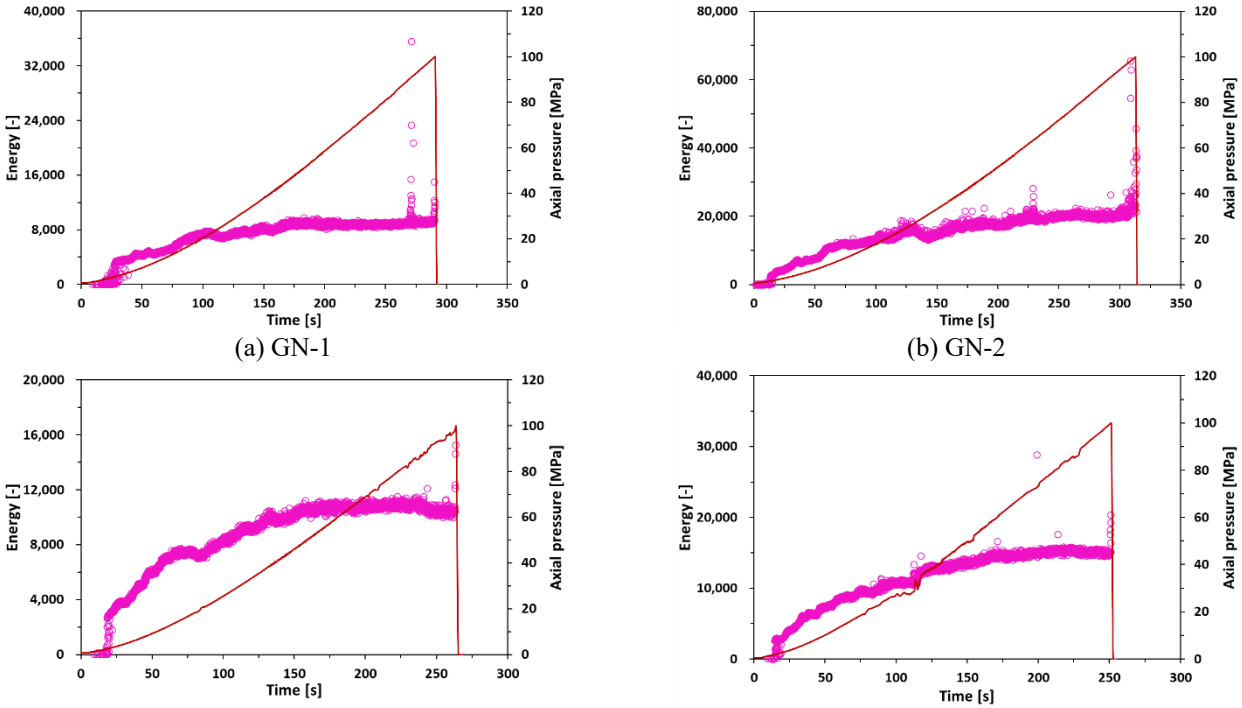

Fig. 5 Energy results for all test specimens under axial pressure

3.1 Count

The AE parameter, count [-], is defined as the number of oscillations of a signal above the threshold voltage in an AE waveform. The threshold voltage is the minimum level required to capture an AE signal, and the amplitude must exceed this level to be recorded. The count increased as the axial pressure in all test specimens increased (Fig. 4). Notably, a significant increase in the count occurred in the range of 3,000–18,000 when cracks occurred in all specimens.

The count tended to be higher in granite than in gabbro or slate during the axial loading test. For specimens GN-1 and GN-2, the count was measured in the range of 3,000–5,000 under axial loading conditions. The count was to be in the range of 2,000–3,000 for GB and SL specimens. Furthermore, the tendency of the count to suddenly increase with the occurrence of cracks was more clearly observed in the granite specimens than in the gabbro and slate specimens. When a crack occurred in the granite specimens, the count was measured in the range of 6,000–18,000 for both GN-1 and GN-2. The count was measured in the range of 3,000–5,000 for GB and 3,000–6,000 for SL.

Based on these results, we concluded that the count tends to decrease as the elastic modulus, that is, Young's modulus increases (GN < GB and SL). As Young's modulus increased, the samples exhibited greater resistance to deformation under external loads. In cases of higher elastic modulus, large-scale failure predominantly occurs at ultimate failure owing to a load increase rather than the continuous occurrence of small-scale deformation (Petružálek *et al*. 2019, Wang *et al*. 2020). In contrast, small-scale deformation occurred continuously under the loading conditions when the elastic modulus was lower. In this study, an axial pressure of up to 100 MPa was applied to evaluate the AE characteristics of the microcracks in the specimens. Therefore, the count value in GN were higher than those in GB and SL.

3.2 Energy

The AE parameter, energy [-], is defined as the area under the detected AE waveform envelop. Fig. 5 shows the variation in energy according to the axial pressure for all test specimens. The results indicate that during the axial loading test the energy increased in the range of 10,000–70,000 when a crack occurred.

The tendency of the energy variation is similar to that of the count variation resulting from axial pressure. When the axial pressure increased, the energy increased to approximately 8,000 (GN-1) and 20,000 (GN-2). The measured energy was within the range of 8,000–10,000 for the GB specimens and 10,000–15,000 for the SL specimens.

Higher energy values were observed in the specimens under axial loading conditions when cracks occurred. The energy values were in the ranges of 10,000–36,000 for GN-1 and 20,000–70,000 for GN-2. For the GB and SL specimens, the energy values were 12,000–16,000 and 15,000–20,000 when cracks occurred, respectively. This tendency can be explained by the differences in elastic moduli of the rocks, which is consistent with the trend observed in the count parameter analysis. Under lower loading conditions (microcrack occurrence), deformation is more noticeable in rocks characterized by a lower elastic modulus than in those with a higher elastic modulus. Consequently, this distinctive behavior resulted in higher energy values in GN-1 and GN-2 than in GB and SL.

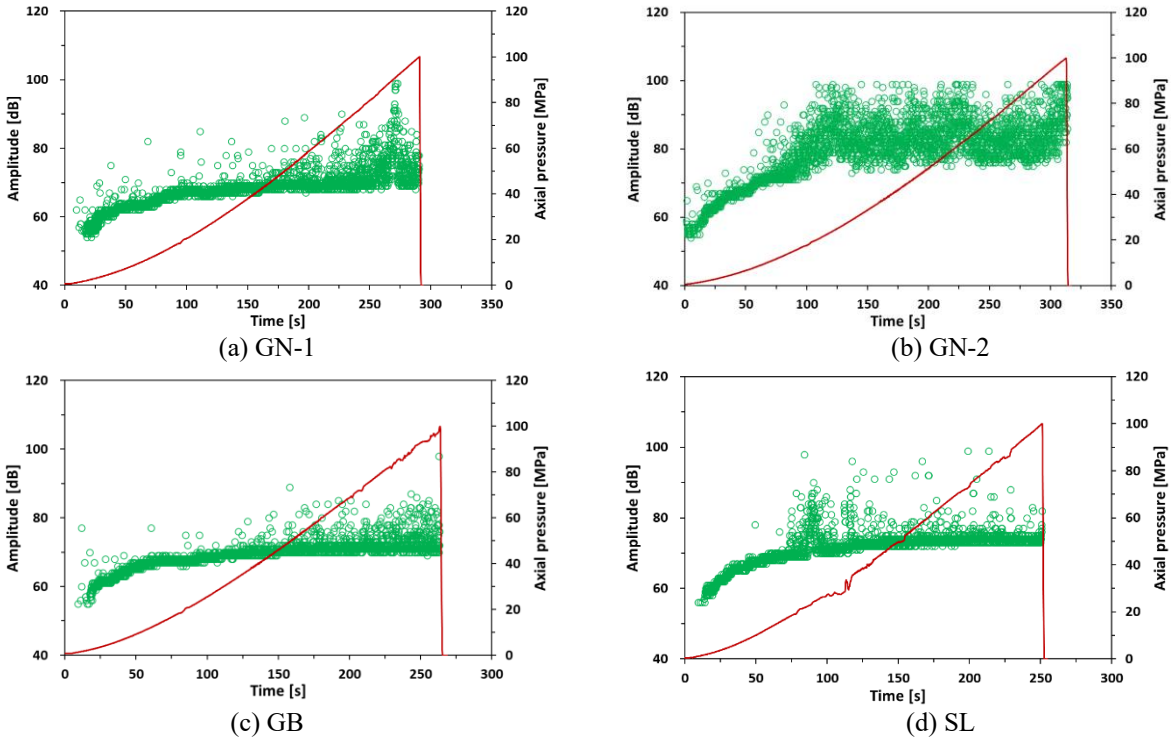

Fig. 6 Amplitude results for all test specimens under axial pressure

3.3 Amplitude

The AE parameter, amplitude [dB], represents the maximum voltage in the AE waveform. In this study, a threshold level of 54 dB was set to consider environmental effects (e.g., noise) in the laboratory, and the AE measurement system could measure AE signals with a maximum amplitude of up to 100 dB. Therefore, the measurable range of amplitude was from 54 to 100 dB.

The amplitude increased in all test specimens as the axial pressure increased (Fig. 6). The amplitude range was measured in the range of 60–70 dB for GN-1 and 60–80 dB for GN-2 with an increase in axial pressure. Similarly, the amplitude for the GB and SL specimens were measured in the ranges of 60–70 and 60–75 dB, respectively.

A significant increase in amplitude was observed in the specimens when cracks occurred because of axial loading, particularly in those with a lower Young's modulus (GN-1 and GN-2). In specimens GN-1 and GN-2, the amplitude ranged from 80 to 100 dB during crack occurrence with an axial loading of up to 100 MPa. In the GB and SL specimens, the amplitudes ranged from 70–85 and 75–90 dB, respectively. This observed amplitude trend is similar to the findings of the count and energy analyses. In the case of specimens with a low elastic modulus, significant large-scale deformation occurred before the ultimate failure of the specimen.

3.4 Average frequency

The AE parameter, average frequency [kHz], was determined by dividing the count by the duration, as shown in Fig. 3. A slight increase in the average frequency was observed in the early stages (elapsed time of 0–100 s) of applying an axial load to the test specimens. No significant changes were observed thereafter (Fig. 7). The average frequency increased to 20 kHz for GN-1 and 30 kHz for GN-2 during the first 100 s of the axial loading test. Subsequently, the average frequencies for GN-1 and GN-2 increased to approximately 25 and 40 kHz, respectively. Similar trends were observed in the GB and SL specimens, where the average frequencies increased to 25 and 30 kHz, respectively, within the first 50 s of the axial loading test and subsequently converged within the range of 25–35 kHz.

The average frequency increased with the occurrence of cracks induced by axial pressure in the specimens, particularly in those with a lower Young's modulus. The average frequency ranged from 40–170 kHz when cracks occurred in specimens GN-1 and GN-2. Meanwhile, the average frequencies of the GB and SL specimens were measured in the range of 35–60 kHz. Despite these observations, there was no significant change in the average frequency compared to the count, energy, and amplitude parameters.

3.5 RA value

The AE parameter, RA value [ms/V], was obtained by dividing the rise time by the amplitude. The RA value decreased as the axial pressure in all test specimens increased, as shown in Fig. 8. During the early stages (first 50 s) of the axial loading test, the RA value was observed to have a wide range from approximately 0–80 ms/V. However, the subsequent application of an axial load resulted in a decrease in the RA value to below 20 ms/V.

The GN-1 and GN-2 specimens showed RA value ranges of approximately 0–60 and 0–70 ms/V, respectively,

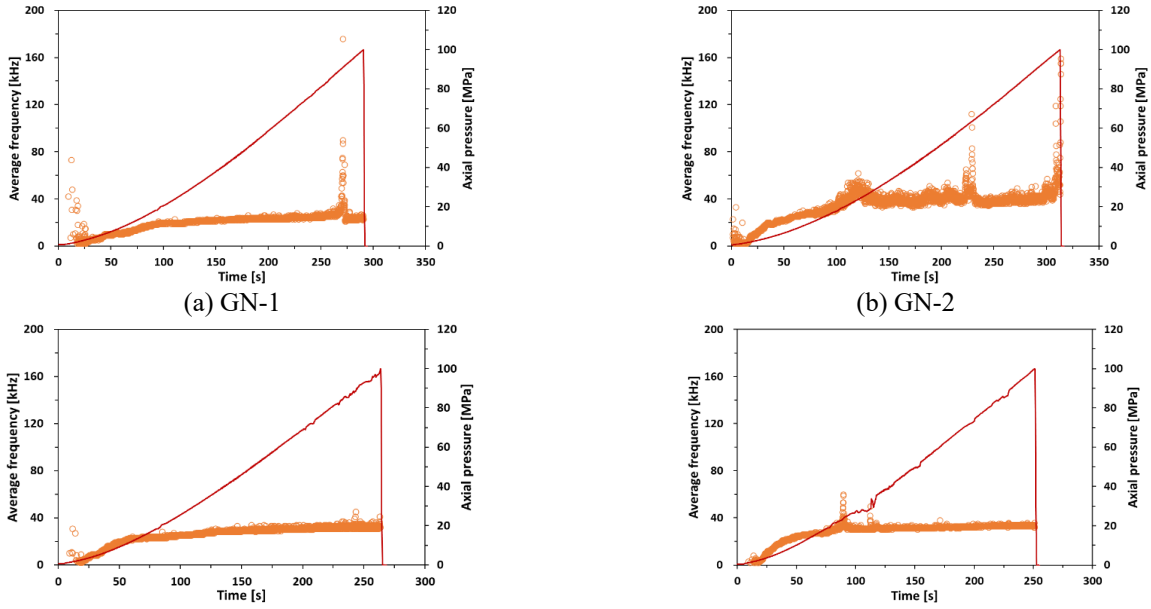

(a) GN-1 (b) GN-2

(c) GB (d) SL

Fig. 7 Average frequency results for all test specimens under axial pressure

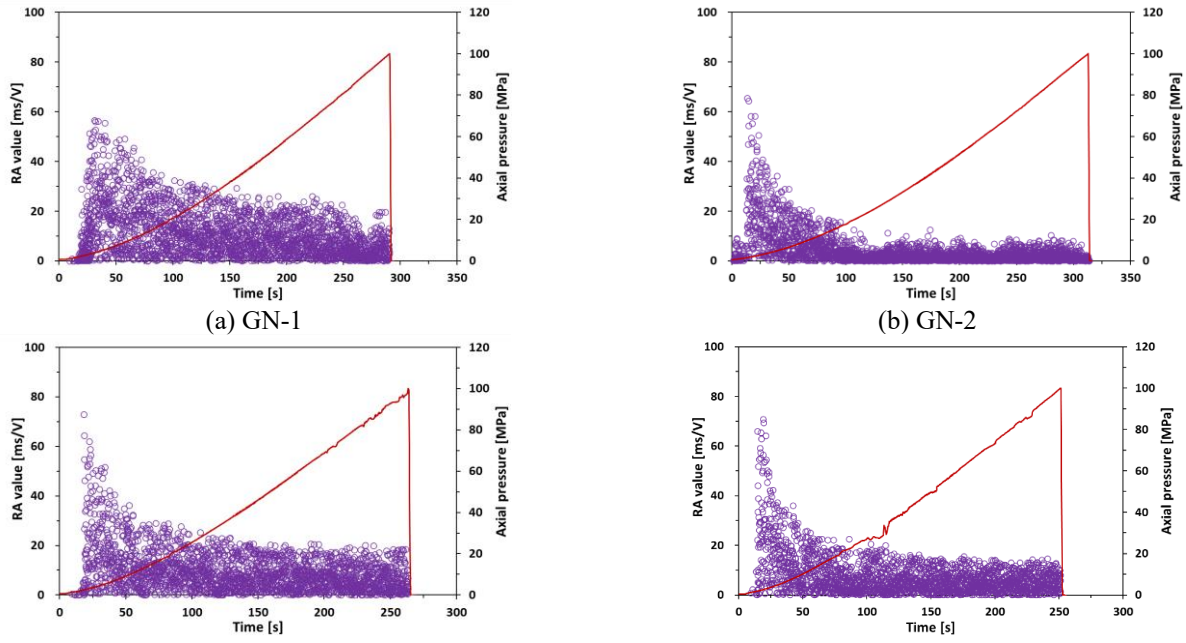

(a) GN-1 (b) GN-2

(c) GB (d) SL

Fig. 8 RA value results in all test specimens under axial pressure

before 50 s of axial loading. Thereafter, the RA value range decreased to 0–30 ms/V for GN-1 and 0–10 ms/V for GN-2. These trends were also observed in the GB and SL specimens. With an increase in the axial load, the RA values of the GB and SL specimens were approximately 0–80 ms/V (first 50 s) and 0–20 ms/V (after 50 s).

The decrease in RA with increasing axial pressure is considered to be a change in the failure mode. AE signals with low RA values are associated with tensile failure (crack opening), whereas those with high RA values are associated with shear failure (crack sliding), based on the crack opening mechanism (Fig. 9). Therefore, the decrease in RA with increasing axial pressure can be explained by the generation of more tensile cracks than shear cracks in the specimens.

4. Discussion

4.1 Localization of damaged zone

The source location algorithm can determine the

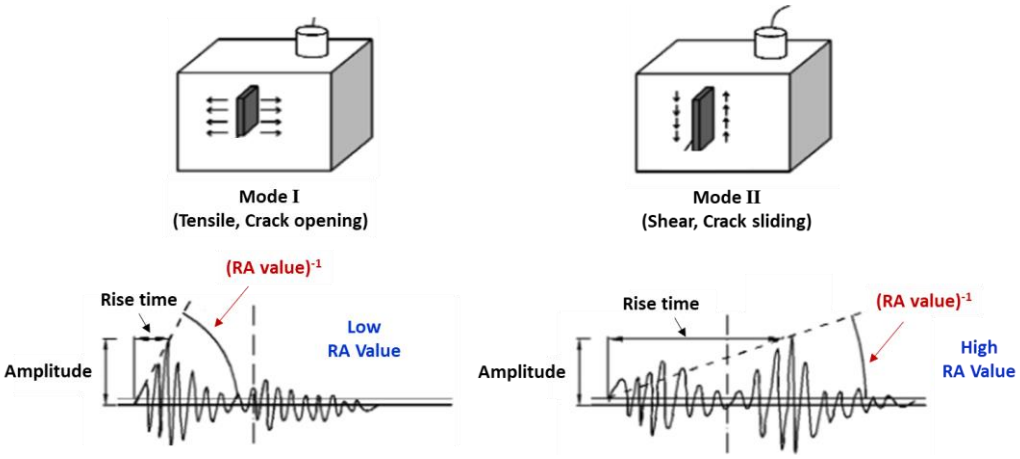

Fig. 9 RA value characteristics according to tensile and shear failure (Lacidogna *et al*. 2017)

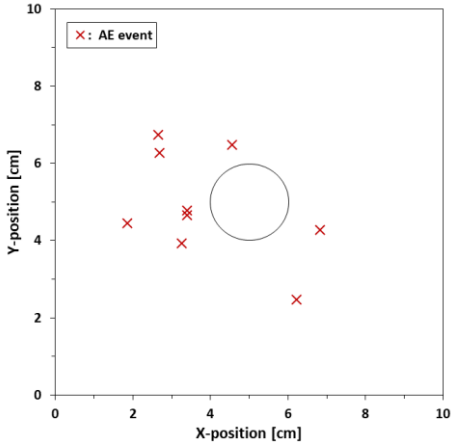

(a) Source location by AE system

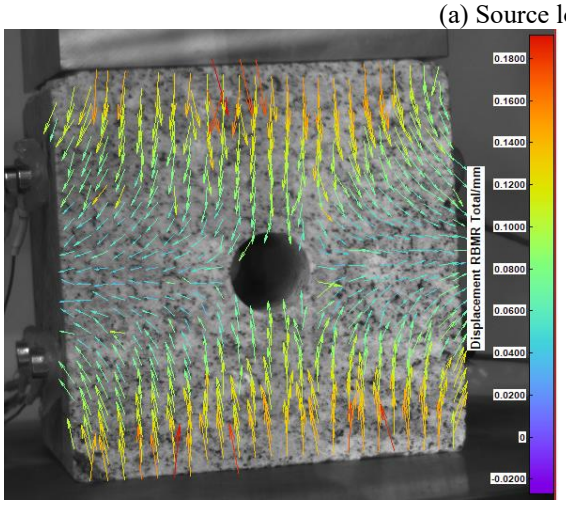

(b) Displacement result by DIC camera

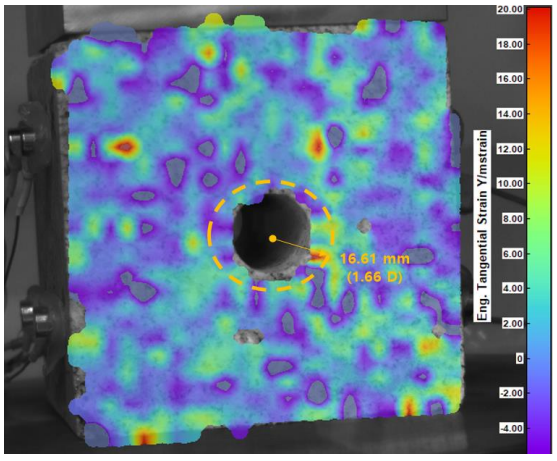

(c) Tangential strain result by DIC camera

Fig. 10 Damage localization of the GN-1 specimen

location of an AE signal based on data collected from at least three AE sensors that form a cluster using the arrival time–distance relationship, which is based on the velocity of sound waves (Dong *et al*. 2022). A source location algorithm was implemented in the AE monitoring system to assess the damaged zone formation and its influence range induced by the experimental loading conditions. The coordinates of the four AE sensors and dimensions of the specimens were used to define the interpretation domain of the algorithm. The built-in function of the AEwin software was used to estimate the two-dimensional source location. In addition, the relationship between amplitude and propagation distance decay was considered in the function. The source location results revealed that GN-1 exhibited

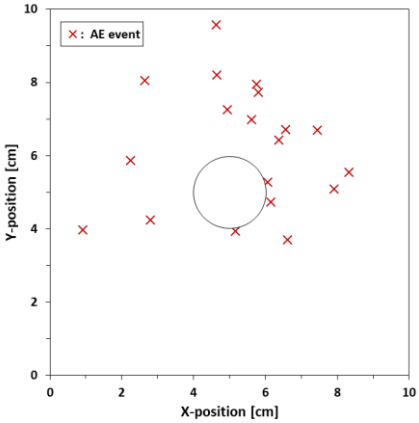

(a) Source location by AE system

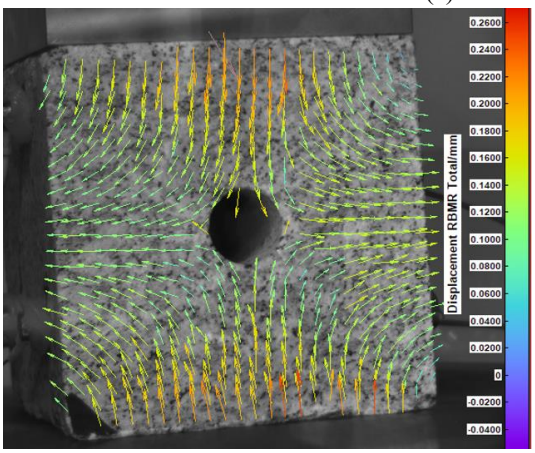

(b) Displacement result by DIC camera

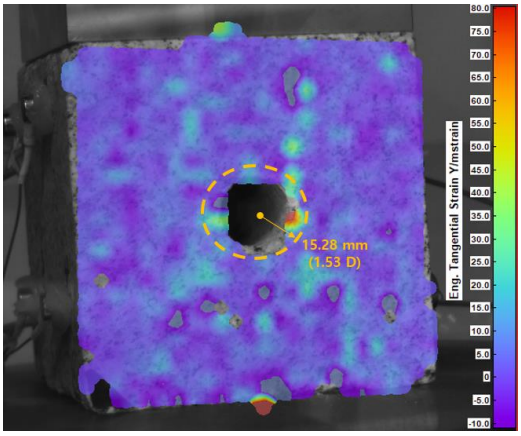

(c) Tangential strain result by DIC camera

Fig. 11 Damage localization of the GN-2 specimen

nine AE events, whereas GN-2 exhibited 20 AE events. Similarly, the source location of GB and SL showed 19 and 21 AE events, respectively. These AE events were attributed to the internal defects of the specimens, indicating a spatial distribution of microcracks and including the formation of a damaged zone under an external axial load. The number of AE events reveals an inverse relationship with the rock strength. Thus, a relatively low number of total AE events in SL were recorded owing to its high uniaxial compression strength. Conversely, the occurrence of five AE events directly adjacent to the circular openings in SL indicates that stress and the resulting damage were concentrated near the circular opening, signifying the formation of a damaged zone. Similarly, GN-1, GN-2, and GB exhibited one, three, and one AE events near the circular openings, respectively, indicating that a damaged zone had formed during the experiments.

Figs. 10-13 show the vector of the total displacement rigid body motion removal (RBMR) and strain contour in the DIC analysis domain based on the specimen types. In all specimens, the vector quiver showed that compression occurred in the axial direction around the opening, whereas tension occurred in the perpendicular direction, indicating stress redistribution because of the loading applied to the circular opening. The strain contour shows that the high-tangential strain region is concentrated around the circular openings. This phenomenon implies that a damaged zone formed near the hole; the influential diameter is indicated in red in Figs. 10-13. The estimated diameters of the damaged zone compared initial diameter (D) for GN-1, GN-2, GB, and SL were 1.66D, 1.53D, 1.49D, and 1.9D, respectively. The average displacements at the surface of the damaged zone for GN-1, GN-2, GB, and SL were 0.814, 0.786, 0.661, and 0.673 mm, respectively, demonstrating a strong correlation with Young's modulus, as shown in Fig. 14.

The concentrated damage patterns near the hole in SL are attributed to the relatively uniform mineral composition and consistent mineralogical structure. This caused the stress concentration near the hole to have a dominant effect on the AE and DIC monitoring results of SL compared to those of the GN and GB. In contrast, the scattered and random distribution of tangential strain in GN and GB can be explained by the presence of heterogeneities, such as variations in mineral content and structural features (Deer *et al*. 2013, Marshak 2019). This phenomenon is in good agreement with the AE event distributions, implying that the AE and DIC techniques can be unified for evaluating damaged zones around circular openings. Thus, the DIC monitoring results indicate that the parameter-based characteristics of AE in Section 3 can be attributed to the evolution of the damaged zone.

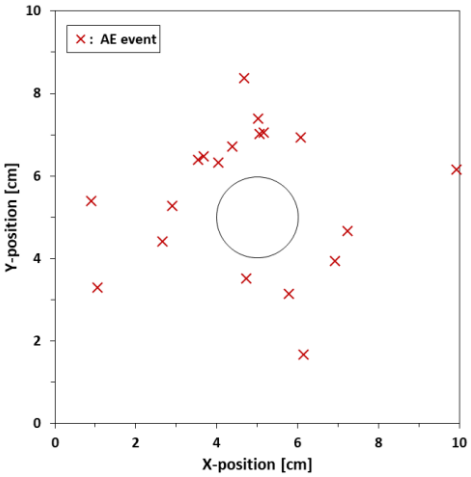

(a) Source location by AE system

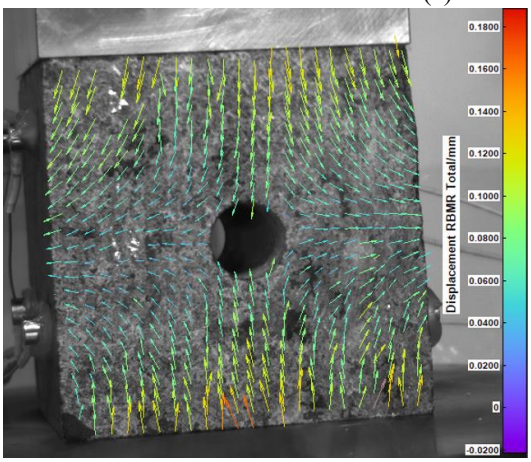

(b) Displacement result by DIC camera

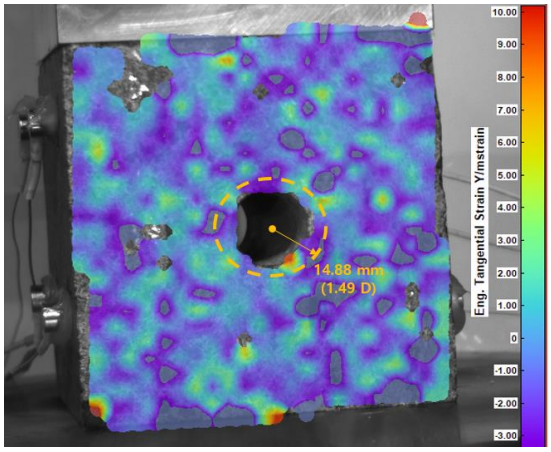

(c) Tangential strain result by DIC camera

Fig. 12 Damage localization of the GB specimen

4.2 AE characteristics with failure mode in circular openings

Deformation is dependent on the stress distribution in the surrounding rock when a damaged zone, such as a circular opening in a rock medium, is generated. The principal stress in the rock medium is composed of three-dimensional components: maximum, intermediate, and minimum stresses. When the stress applied to the boundary of the damaged zone exceeds the strength of the rock, tensile cracks occur along the direction of the maximum principal stress, which is perpendicular to the direction of the minimum principal stress (Aliabadian *et al*. 2019). Analyzing the characteristics of tensile crack development to ensure underground rock stability is necessary because the tensile strength of rocks is significantly smaller than their compressive strength (Perras and Diederichs 2016).

In previous studies, the failure mode of rocks was analyzed using the AE monitoring technique (Li *et al*. 2017). The failure mode can be divided into tensile and shear failures, which can be analyzed using the AE parameters, RA value and average frequency. In the failure mode analysis, based on the AE characteristics, the AE signals were characterized by low RA values and high average frequencies in tensile failure, whereas they were characterized by high RA values and low average frequencies in shear failure. As shown in Fig. 15, the failure mode can be distinguished by utilizing a criterion, that is, the graphical line showing the relationship between the RA value and average frequency. The slope of the criterion varies depending on the rock type, geometry, and loading conditions (Du *et al*. 2020, Liu *et a*l. 2020).

In this study, axial loading tests were conducted on rock specimens with circular openings to evaluate their AE characteristics during crack occurrences. The maximum loading level was set to 100 MPa to analyze microcrack generation in the specimens. After testing, the elapsed loading time was investigated for approximately 300 s for all specimens. To analyze the failure mode with an increase in axial pressure and identify the crack development characteristics through the RA value and average frequency, three subsequent steps were taken: first ($t < 100$ s), second ($100 \text{ s} < t < 200$ s), and final ($t > 200$ s).

Based on the axial loading test results, Fig. 16 presents the variation in RA value and average frequency with elapsed loading time: first ($t < 100$ s, blue dots), second ($100 \text{ s} < t < 200$ s, green dots), and final ($t > 200$ s, red dots). The RA values exhibited a decreasing trend for all

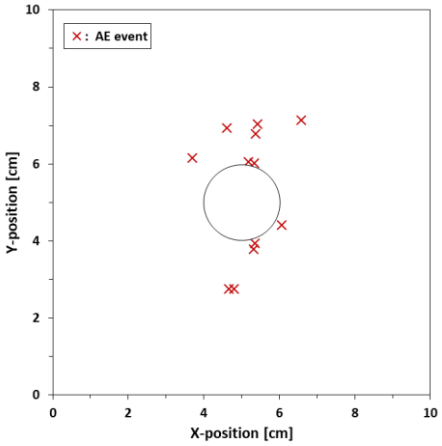

(a) Source location by AE system

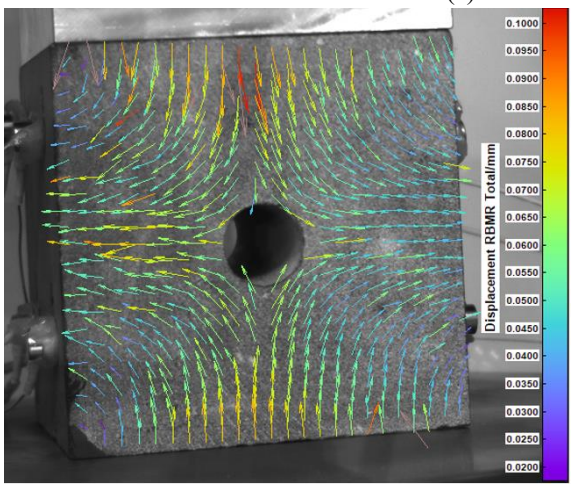

(b) Displacement result by DIC camera

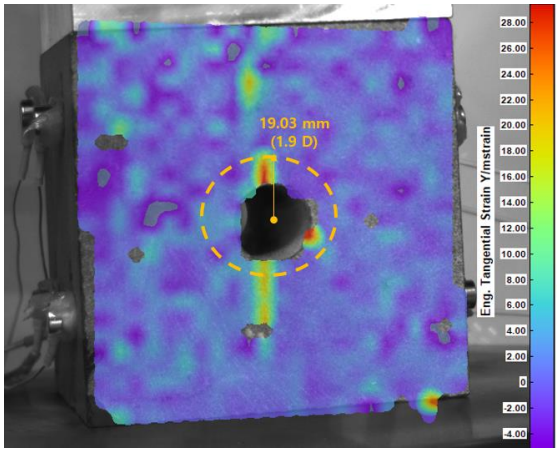

(c) Tangential strain result by DIC camera

Fig. 13 Damage localization of the SL specimen

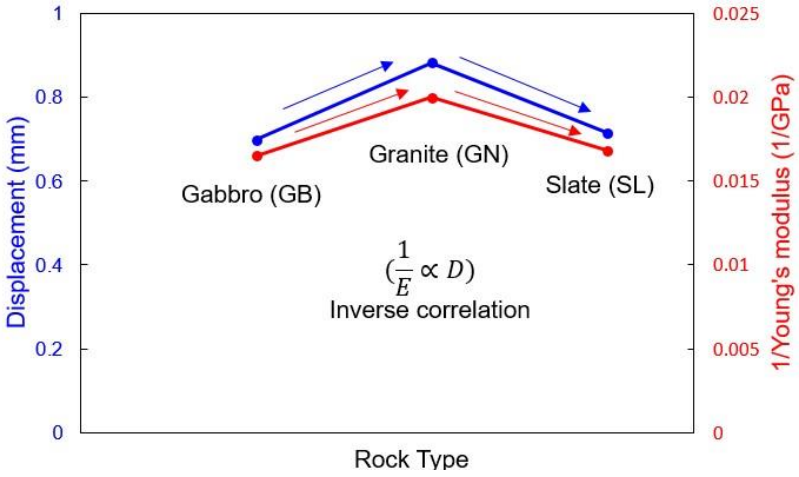

Fig. 14 Correlation between the average displacement and Young's modulus

specimens when the axial pressure increased. In GN-1 and GN-2, the RA values decreased within the ranges of 0–65 ms/V (first), 0–32 ms/V (second), and 0–26 ms/V (final). Similarly, the RA values for the GB and SL specimens decreased within the ranges of 0–72 ms/V (first), 0–25 ms/V (second), and 0–20 ms/V (final).

In contrast, all specimens showed an increasing trend in the average frequency. As the axial pressure increased, the average frequency for specimens GN-1 and GN-2 increased in the ranges of 2–37 kHz (first), 31–62 kHz (second), and 34–176 kHz (final). Furthermore, the average frequencies of the GB and SL specimens increased within the ranges of

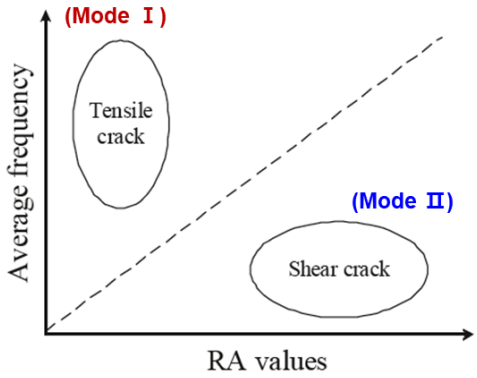

Fig. 15 Crack classification according to the RA value and average frequency (after Grosse and Ohtsu 2008)

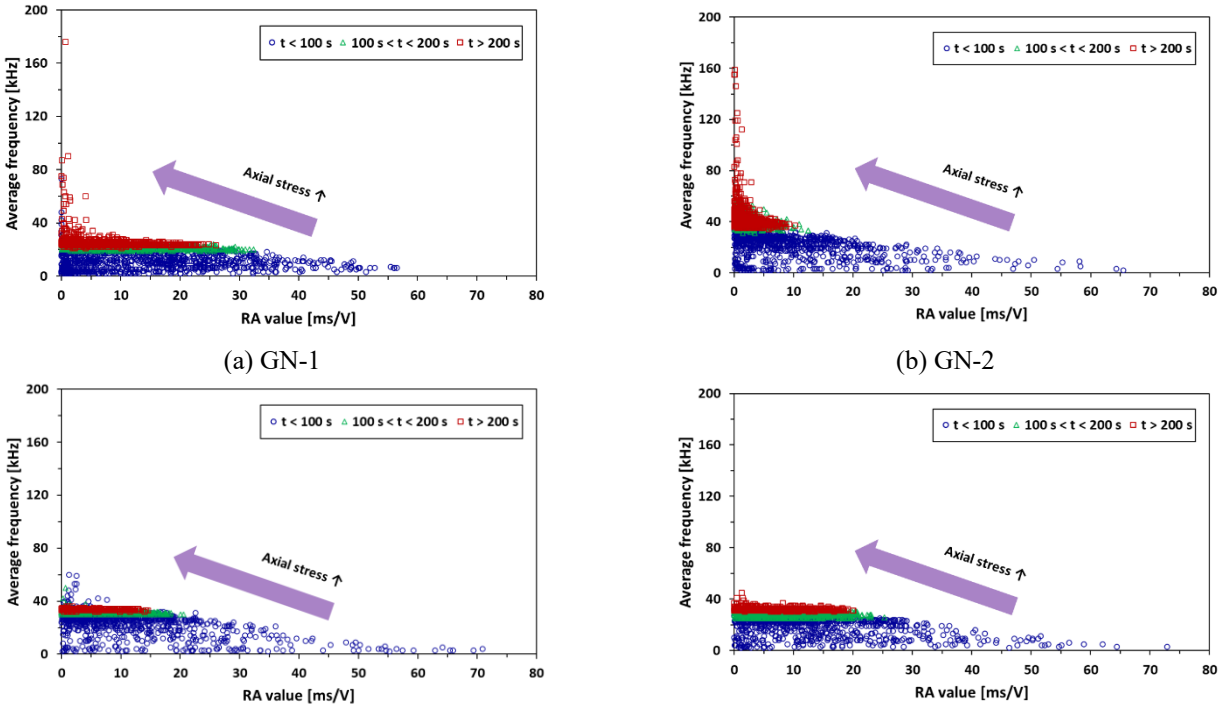

(a) GN-1 (b) GN-2

(c) GB (d) SL

Fig. 16 Relationship between the RA value and average frequency according to elapsed axial loading time

2–30 kHz (first), 25–34 kHz (second), and 32–45 kHz (final). Table 2 lists the detailed values of RA and average frequency according to the elapsed loading time.

Given these tendencies, we suggest that an increase in the maximum principal stress could generate more tensile cracks. The failure mode analysis, based on the AE characteristics, indicated that the occurrence of a tensile crack could be identified by an AE signal with a low RA value and high average frequency. In this study, the AE signals revealed that shear cracks were primarily generated during the first step (<100 s), as indicated by the high RA values and low average frequencies (blue dots in Fig. 16). However, as the elapsed loading time steps progressed (first to final), tensile cracks gradually generated from the AE signals and were identified by the low RA values and high average frequencies (red dots in Fig. 16).

These characteristics were identified through the DIC analyses over time during the uniaxial loading tests. Fig. 17 shows an example of the vector of the total displacement RBMR measured in GN-1 during the uniaxial loading test. In the first step (t < 100 s), the vectors were irregular within the rock medium under the loading conditions (Figs. 17(a) and 17(b)). These irregular patterns were induced by the closure of pores or cracks within the specimen. Subsequently, during the second step (100 s < t < 200 s) and final step (t > 200 s), the vectors exhibited a distinct formation trend in the vertical (axial) direction under the loading conditions (Fig. 17(c) and 17(d)). This indicates that tensile failure occurred predominantly when the axial load increased along the maximum principal direction. This analysis utilizing the AE technique with a DIC camera system can monitor the stability of underground rocks.

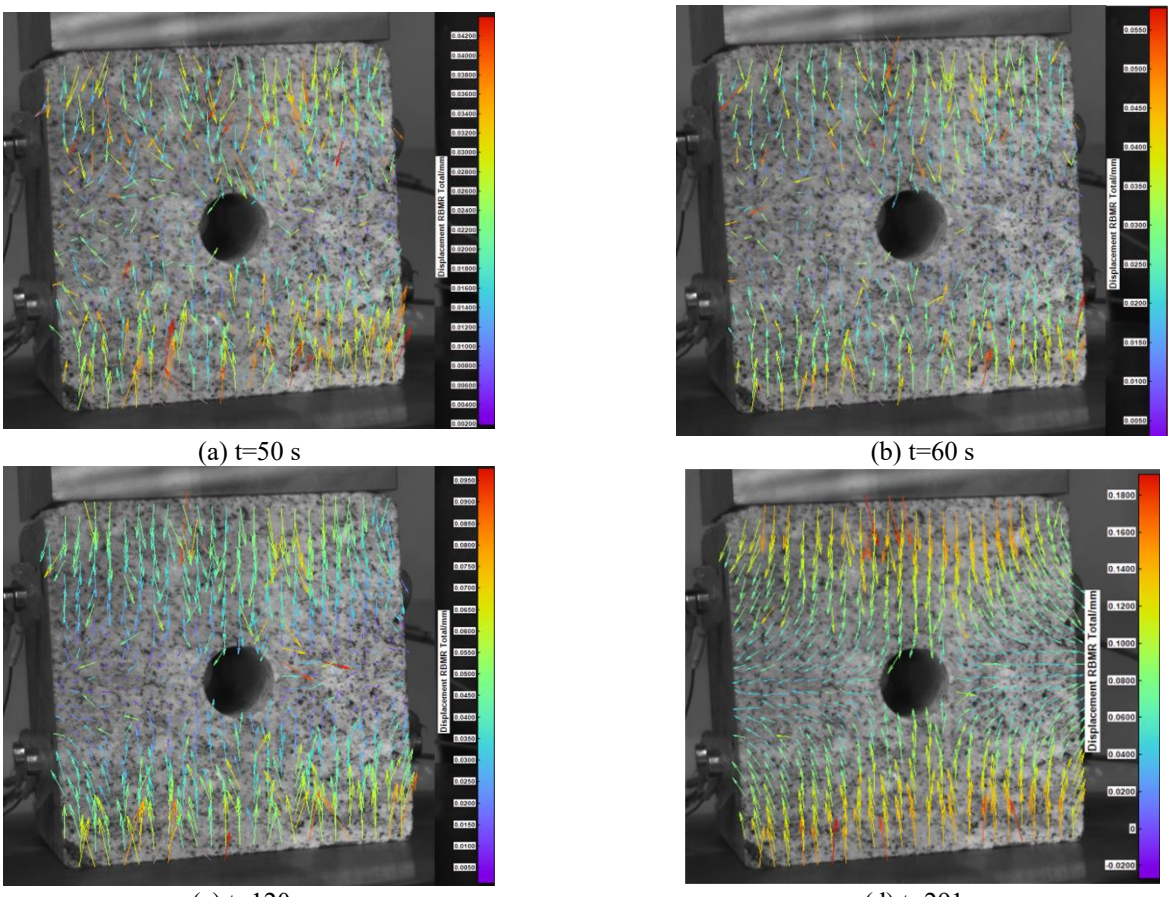

(a) t=50 s (b) t=60 s

(c) t=120 s (d) t=291 s

Fig. 17 Example of total displacement vector in GN-1 over time during the uniaxial test

Table 2 RA value and average frequency according to loading time for all test specimens

AE parameter	Specimen	Loading time		
		t < 100 s	100 s ≤ t < 200 s	t ≥ 200 s
RA value [ms/V]	GN-1	0.00 to 56.51(15.6)*	0.02 to 32.40(10.6)	0.02 to 26.06(7.0)
	GN-2	0.01 to 65.48(10.1)	0.00 to 12.49(2.1)	0.00 to 10.27(1.9)
	GB	0.00 to 72.87(14.2)	0.00 to 25.25(8.3)	0.02 to 20.09(6.9)
	SL	0.03 to 70.93(12.0)	0.01 to 20.51(6.0)	0.01 to 14.60(5.4)
Average frequency [kHz]	GN-1	2 to 73(10.7)	19 to 26(21.7)	21 to 176(25.6)
	GN-2	2 to 37(20.8)	31 to 62(40.4)	34 to 159(42.7)
	GB	2 to 31(18.8)	25 to 34(28.7)	30 to 45(32.2)
	SL	2 to 60(22.7)	30 to 50(31.7)	32 to 36(33.4)

5. Conclusions

In civil engineering, the utilization of underground spaces has played a significant role in the construction of important social infrastructures, such as deep geological repositories. The damaged zone can be a potential risk to the mechanical stability of underground spaces. Therefore, reliable monitoring techniques are necessary to evaluate damage and integrity. In this study, the applicability of the AE technique was analyzed as a suitable method for damage detection in rock media. To achieve this objective, uniaxial stress tests were performed on circular opening specimens using an AE monitoring system. The main findings of this study are summarized as follows.

• The AE characteristics were analyzed by evaluating various AE parameters, including count, energy, amplitude, average frequency, and RA value. The count, energy, and amplitude parameters increased as the axial stress increased. Furthermore, these parameter values considerably increased when cracks occurred during the uniaxial compression test in the specimens with a lower Young's modulus.

• The average frequency slightly increased when the uniaxial stress increased, although the changes were insignificant. In contrast, the RA value showed a decreasing trend with an increase in uniaxial stress. This observation indicates that a higher uniaxial stress leads to a greater generation of tensile cracks.
• Based on the damage localization determined using the AE system, cracks occurred along the axial load direction. The displacement and tangential strain were measured using a DIC camera to validate the crack occurrence patterns. The observed crack occurrence patterns were consistent with the results obtained from the AE system. These results confirm that the AE monitoring technique can effectively detect damage in rock media.
• Through the failure mode analysis using the RA value and average frequency, the observed cracks along the axial load direction, as identified by the AE system and DIC camera, were determined to be tensile cracks. Furthermore, there was a higher occurrence of tensile cracks than shear cracks with an increase in uniaxial stress.

We expected this study to be valuable for reliable damage monitoring using the AE technique in damaged zones around circular openings.

Acknowledgments

This work was supported by the Basic Research Project of the Korea Institute of Geoscience and Mineral Resources (KIGAM, GP2020-010) funded by the Ministry of Science and ICT, Institute for Korea Spent Nuclear Fuel (iKSNF), and Korea Foundation of Nuclear Safety (KOFONS) grant funded by the Korean government (Nuclear Safety and Security Commission, NSSC) [grant number RS-2021-KN066110]. This research was also conducted as part of the Brain Korea 21 FOUR Project at the Education & Research Center for the Infrastructure of the Smart Ocean City (i-SOC Center).

References

AEwin (2014), Software Users' Manual, MISTRAS Group Inc., Benicia, CA, USA.

Aliabadian, Z., Zhao, G.F. and Russell, A.R. (2019), "Failure, crack initiation and the tensile strength of transversely isotropic rock using the Brazilian test", *Int. J. Rock Mech. Min. Sci.*, **122**, 104073. https://doi.org/10.1016/j.ijrmms.2019.104073.

ASTM D2845-08 (2008), Standard test method for laboratory determination of pulse velocities and ultrasonic elastic constants of rock, ASTM International, West Conshohocken, PA, USA.

ASTM D7012-10 (2010), Standard test method for compressive strength and elastic moduli of intact rock core specimens under varying states of stress and temperatures, ASTM International, West Conshohocken, PA, USA.

ASTM D-7063 (2011), Standard test method for effective porosity and effective air voids of compacted bituminous paving mixture samples, ASTM International, West Conshohocken, PA, USA.

Cao, A., Jing, G., Ding, Y.L. and Liu, S. (2019), "Mining-induced static and dynamic loading rate effect on rock damage and acoustic emission characteristic under uniaxial compression", *Saf. Sci.,* **116**, 86-96. https://doi.org/10.1016/j.ssci.2019.03.003.

Du, K., Li, X., Tao, M. and Wang, S. (2020), "Experimental study on acoustic emission (AE) characteristics and crack classification during rock fracture in several basic lab tests", *Int. J. Rock Mech. Min. Sci.*, **133**, 104411. https://doi.org/10.1016/j.ijrmms.2020.104411.

Du, K., Sun, Y., Zhou, J., Khandelwal, M. and Gong, F. (2022), "Mineral composition and grain size effects on the fracture and acoustic emission (AE) characteristics of rocks under compressive and tensile stress", *Rock Mech. Rock Eng.*, **55**, 6445-6474. https://doi.org/10.1007/s00603-022-02980-y.

Deer, W.A., Howie, R.A. and Zussman, J. (2013), An introduction to the rock-forming minerals, 3rd Ed., Longman, Harlow, UK.

Dong, L., Yang, L., Chen, Y. (2022), "Acoustic emission location accuracy and spatial evolution characteristics of granite fracture in complex stress conditions", *Rock Mech. Rock Eng.*, **56**(6), 1–18. https://doi.org/10.1007/s00603-022-03124-y.

Fakhimi, A., Carvalho, F., Ishida, T. and Labuz, J.F. (2002), "Simulation of failure around a circular opening in rock", *Int. J. Rock Mech. Min. Sci.*, **39**(4), 507-515. https://doi.org/10.1016/S1365-1609(02)00041-2.

Gong, Y., Song, Z., He, M., Gong, W. and Ren, F. (2017), "Precursory waves and eigenfrequencies identified from acoustic emission data based on singular spectrum analysis and laboratory rock-burst experiments", *Int. J. Rock Mech. Min. Sci.*, **91**, 155-169. https://doi.org/10.1016/j.ijrmms.2016.11.020.

Grosse, C.U. and Ohtsu, M. (2008), Acoustic emission testing, Springer, Heidelberg, Germany.

Guo, W.Y., Zhang, W., Zhang, C.G. and Chen, Y. (2022a), "Experimental study on the deformation localisation and acoustic emission characteristics of coal in Brazilian splitting tests", *Sci. Rep.*, **12**, 6348. https://doi.org/10.1038/s41598-022-10332-7.

Guo, T.Y. and Zhao, Q. (2022b), "Acoustic emission characteristics during the microcracking processes of granite, marble and sandstone under mode 1 loading", *Rock Mech. Rock Eng.*, **55**, 5467-5489. https://doi.org/10.1007/s00603-022-02937-1.

Hampton, J., Gutierrez, M., Matzar, L., Hu, D. and Frash, L. (2018), "Acoustic emission characterization of microcracking in laboratory-scale hydraulic fracturing tests", *J. Rock Mech. Geotech. Eng.*, **10**, 805–817. https://doi.org/10.1016/j.jrmge.2018.03.007.

Hedayat, A. and Weems, J. (2019), "The elasto-plastic response of deep tunnels with damaged zone and gravity effects", *Rock Mech. Rock Eng.*, **52**, 5123-5135. https://doi.org/10.1007/s00603-019-01834-4.

Hellier, C.J. (2013), Handbook of nondestructive evaluation, McGraw-Hill Education, New York, NY, USA.

Ishida, T., Labuz, J.F., Manthei, G., Meredith, P.G., Nasseri, M.H.B., Shin, K., Yokoyama, T. and Zang, A. (2017), "ISRM suggested method for laboratory acoustic emission monitoring", *Rock Mech. Rock Eng.*, **50**, 665-674. https://doi.org/10.1007/s00603-016-1165-z.

Jin, P., Wang, E. and Song, D. (2017), "Study on correlation of acoustic emission and plastic strain based on coal-rock damage theory", *Geomech. Eng.*, **12**(4), 627-637. https://doi.org/10.12989/gae.2017.12.4.627.

Kramadibrata, S., Simangunsong, G.M., Matsui, K. and Shimada, H. (2011), "Role of acoustic emission for solving rock engineering problems in Indonesian underground mining", *Rock Mech. Rock Eng.*, **44**, 281-289. https://doi.org/10.1007/s00603-010-0125-2.

Lacidogna, G., Piana, G. and Carpinteri, A. (2017), "Acoustic emission and modal frequency variation in concrete specimens under four-point bending", *Appl. Sci.*, **7**(4), 339. https://doi.org/10.3390/app7040339.

Lee, J.W., Kim, H. and Oh, T.M. (2020), "Acoustic emission

characteristics during uniaxial compressive loading for concrete specimens according to sand content ratio", *KSCE J. Civ. Eng.*, **24**(9), 2808-2823. https://doi.org/10.1007/s12205-020-5697-0.

Li, L.R., Deng, J.H., Zheng, L. and Liu, J.F. (2017), "Dominant frequency characteristics of acoustic emissions in white marble during direct tensile tests" *Rock Mech. Rock Eng.*, **50**, 1337-1346. https://doi.org/10.1007/s00603-016-1162-2.

Li, J., Shen, C., He, X., Zheng, X. and Yuan, J. (2022a), "Numerical solution for circular tunnel excavated in strain-softening rock masses considering damaged zone", *Sci. Rep.*, **12**, 4465. https://doi.org/10.1038/s41598-022-08531-3.

Li, C.J., Lou, P.J. and Xu, Y. (2022b), "Damage characterization of hard-brittle rocks under cyclic loading based on energy dissipation and acoustic emission characteristics", *Geomech. Eng.*, **31**(4), 365-373. https://doi.org/10.12989/.2022.31.4.365.

Li, S., Yang, D., Huang, Z., Gu, Q. and Zhao, K. (2022c), "Acoustic emission characteristics and failure mode analysis of rock failure under complex stress state", *Theor. Appl. Fract. Mec.*, **122**, 103666. https://doi.org/10.1016/j.tafmec.2022.103666.

Liu, J.P., Li, Y.H., Xu, S.D., Xu, S., Jin, C.Y. and Liu, Z.S. (2015), "Moment tensor analysis of acoustic emission for cracking mechanisms in rock with a pre-cut circular hole under uniaxial compression", *Eng. Frac. Mech.*, **135**, 206-218. https://doi.org/10.1016/j.engfracmech.2015.01.006.

Liu, X., Liu, Z., Li, X., Gong, F. and Du, K. (2020), "Experimental study on the effect of strain rate on rock acoustic emission characteristics", *Int. J. Rock Mech. Min. Sci.*, **133**, 104420. https://doi.org/10.1016/j.ijrmms.2020.104420.

Liu, B., Zhao, Y., Zhang, C., Zhou, J., Li, Y. and Sun, Z. (2021), "Characteristic strength and acoustic emission properties of weakly cemented sandstone at different depths under uniaxial compression", *Int. J. Coal Sci. Technol.*, **8**, 1288-1301. https://doi.org/10.1007/s40789-021-00462-0.

Lockner, D. (1993), "The role of acoustic emission in the study of rock fracture", *Int. J. Rock Mech. Min. Sci. Geomec. Abstr.*, **30**(7), 883–899. https://doi.org/10.1016/0148-9062(93)90041-B.

Ma, J., Wu, S., Zhang, X.P. and Gan, Y. (2020), "Modeling acoustic emission in the Brazilian test using moment tensor inversion", *Comput. Geotech.*, **123**, 103567. https://doi.org/10.1016/j.compgeo.2020.103567.

Marshak, S. (2019), Essentials of geology, 6th Ed., W.W. Norton & Company, New York, NY, USA.

Miao, S., Pan, P.Z., Konicek, P., Yu, P. and Liu, K. (2021), "Rock damage and fracturing induced by high static stress and slightly dynamic disturbance with acoustic emission and digital image correlation techniques", *J. Rock Mech. Geotech. Eng.*, **13**, 1002-1019. https://doi.org/10.1016/j.jrmge.2021.05.001.

Moradian, Z., Einstein, H.H. and Ballivy, G. (2016), "Detection of cracking levels in brittle rocks by parametric analysis of the acoustic emission signals", *Rock Mech. Rock Eng.*, **49**, 785-800. https://doi.org/10.1007/s00603-015-0775-1.

Oh, T.M., Kim, M.K., Lee, J.W., Kim, H. and Kim, M.J. (2020), "Experimental investigation on effective distances of acoustic emission in concrete structures", *Appl. Sci.*, **10**(17), 6051. https://doi.org/10.3390/app10176051.

Park, Y.J. and Kim, K.H. (2006), "Analytical solution for a circular opening in an elastic–brittle–plastic rock", *Int. J. Rock Mech. Min. Sci.*, **43**(4), 616-622. https://doi.org/10.1016/j.ijrmms.2005.11.004.

Perras, M.A. and Diederichs, M.S. (2016), "Predicting excavation damage zone depths in brittle rocks", *J. Rock Mech. Geotech. Eng.*, **8**(1), 60-74. https://doi.org/10.1016/j.jrmge.2015.11.004.

Petružálek, M., Lokajíček, T., Svitek, T., Jechumtálová, Z., Kolář, P. and Šílený, J. (2019), "Fracturing of migmatite monitored by acoustic emission and ultrasonic sounding", *Rock Mech. Rock Eng.*, **52**, 47-59. https://doi.org/10.1007/s00603-018-1590-2.

Sun, Y., Yu, F. and Lv, J. (2023), "Experimental study on acoustic emission characteristics of granite and sandstone under uniaxial compression", *Geofluids*, **2023**, 2944871. https://doi.org/10.1155/2023/2944871.

Tang, J.H., Chen, X.D. and Dai, F. (2020), "Experimental study on the crack propagation and acoustic emission characteristics of notched rock beams under post-peak cyclic loading", *Eng. Fract. Mech.*, **226**, 106890. https://doi.org/10.1016/j.engfracmech.2020.106890.

Wang, F. and Qian, D. (2018), "Difference solution for a circular tunnel excavated in strain-softening rock mass considering decayed confinement", *Tunn. Undergr. Sp. Tech.*, **82**, 66-81. https://doi.org/10.1016/j.tust.2018.08.001.

Wang, Z., Wang, J., Yang, S., Li, L. and Li, M. (2020), "Failure behaviour and acoustic emission characteristics of different rocks under uniaxial compression", *J. Geophys. Eng.*, **17**(1), 76-88. https://doi.org/10.1093/jge/gxz092.

Weng, L., Li, X., Taheri, A., Wu, Q. and Xie, X. (2018), "Fracture evolution around a cavity in brittle rock under uniaxial compression and coupled static–dynamic loads", *Rock Mech. Rock Eng.*, **51**, 531-545. https://doi.org/10.1007/s00603-017-1343-7.

Wu, H., Ma, D., Spearing, A.J.S. and Zhao, G. (2021), "Fracture response and mechanisms of brittle rock with different numbers of openings under uniaxial loading", *Geomech. Eng.*, **25**(6), 481-493. https://doi.org/10.12989/gae.2021.25.6.481.

Yoon, S., Jeong, H., Lee, H.L., Kim, T., Hong, C.H. and Kim, J.S. (2023), "Evaluation of Uniaxial Compression and Point Load Tests for Compacted Bentonites", *Acta Geotech.*, **18**, 4633-4644. https://doi.org/10.1007/s11440-023-01844-1.

Zha, E., Zhang, Z., Zhang, R., Wu, S., Li, C., Ren, L., Gao, M. and Zhou, J. (2021), "Long-term mechanical and acoustic emission characteristics of creep in deeply buried jinping marble considering excavation disturbance", *Int. J. Rock Mech. Min. Sci.*, **139**, 104603. https://doi.org/10.1016/j.ijrmms.2020.104603.

Zhang, Z., Hu, L., Liu, T. and Zheng, H. (2021), "Cluster and information entropy analysis of acoustic emission during rock failure process", *Geomech. Eng.*, **25**(2), 135-142. https://doi.org/10.12989/gae.2021.25.2.135.

Zhu, Q., Li, D., Han, Z., Li, X. and Zhou, Z. (2019), "Mechanical properties and fracture evolution of sandstone specimens containing different inclusions under uniaxial compression", *Int. J. Rock Mech. Min. Sci.*, **115**, 33-47. https://doi.org/10.1016/j.ijrmms.2019.01.010.

GC